

<https://doi.org/10.1038/s43247-024-01420-9>

Intermediate-depth seismicity and intraslab stress changes due to outer-rise faulting

Check for updates

Cristina Malatesta ¹✉, Taras Gerya ², Simone Pittaluga¹ & Daniela Cabiddu¹

Intermediate-depth seismicity is common in subducting slabs and the seismicity rate shows some statistically significant yet enigmatic global positive correlation with the maximal throw of outer-rise normal faults. Here, we have simulated the formation and subduction of outer-rise faults, using 2D thermomechanical numerical models of intra-oceanic subduction with coupled brittle-ductile damage of bending plates. We observed that outer-rise faults are formed episodically during slab segmentation and their maximal throw grows with time. When been subducted to intermediate depth, these faults are locally reactivated either by i) slab unbending/bending, simultaneous to the formation of new outer-rise faults or ii) episodic interplate coupling related to the rugged morphology of the faulted downgoing plate. Faults reactivation is concurrent with a local, transient deviatoric stress increase in intraslab domains among these structures. We suggest that slab domains affected by stress increase could be the appropriate location where potential brittle deformation can occur, generating intermediate-depth intraslab earthquakes, that are predominantly localized in heterogeneous regions of dense faulting formed within slab-segments boundaries. The temporal coincidence of stress growth at intermediate depths and throw-growth of, newly-formed, outer-rise faults at the surface may possibly explain the observed global positive correlation of intermediate-depth seismicity rate with maximal fault throw.

Seismic events with focal mechanisms located in the subducting slab are defined as “intraslab earthquakes”.

These events are often distributed along a double seismic zone (DSZ), defining an upper (0–10 km from the subduction interface) and a lower plane (more than 23 km from the subduction interface). Steady seismicity, i.e., excluding aftershocks of large events, has been observed between these two planes, defining interplane events (in between the upper and lower seismic planes, 10–23 km)¹.

In the last decades, a number of scientific works examined the possible mechanisms responsible for their nucleation at intermediate depths (i.e., at depths of 70–300 km)^{2–10}.

Fluids have been suggested to have an important role in triggering earthquakes in the subducting slab. In particular, the occurrence of metamorphic reactions involving dehydration of hydrous minerals in the crust (i.e., MORB dehydration) has been correlated to seismic episodes^{11–16} and, in particular, to seismicity peaks at 80 km depth¹. As an example, in the DDST model (dehydration-driven stress transfer), antigorite breakdown has been invoked as responsible for intermediate depths seismicity in the subducting

oceanic mantle¹⁴: in this model, obtained from studies on synthetic slightly serpentized peridotite, the generation mechanism for intermediate-depth oceanic mantle earthquakes is related to the stress transfer from dehydrating antigorite portions to olivine portions in partially hydrated peridotite, as can occur in a network of serpentized faults cutting fresh peridotite.

Dehydration embrittlement, after increasing fluid pressure in the oceanic lithosphere, has been proposed to trigger, above all, upper-plane and interplane earthquakes, including slow-slip events and episodic tremors close to the plate interface^{1,17–19}. Fluid pressure can increase along preexisting faults, locally reducing their shear strength and triggering instabilities^{12,19,20}. A rupture and a possible earthquake could also nucleate after the interaction, related to an increasing strain, of micro-cracks that formed from originally isolated pockets of water^{12,21}. This mechanism would allow brittle failure to occur at greater depths than would normally be possible¹².

Faccenda et al.²² showed that during slab deserpentinisation, unbending stresses could drive part of the released fluids downward into the cold core of the plate. These fluids can then percolate up-dip along a

¹Institute for Applied Mathematics and Information Technologies, IMATI-CNR, Via De Marini 6, Genoa, Italy. ²Institute of Geophysics, ETH, Sonneggstrasse 5, Zürich, Switzerland. ✉e-mail: cri.malates82@gmail.com

localized layer with zero slab-normal pressure gradients, which form together with the upper hydrated layer located near the top of the slab. The resulting double hydrated zone (DHZ) controls the locations where intermediate-depth seismicity could be triggered. The numerically predicted location and deformation mechanics of the DHZ appeared to be consistent²² with global seismological observations on DSZs²³ and suggests that slab strength, lowering by percolating pressurized fluids, could be the viable mechanism for localization of the observed slab seismicity.

Other triggering mechanisms, such as shear heating or brittle failure due to stress amplification, exclude dehydration reactions: the first mechanism invokes the occurrence of thermal shear instabilities in the oceanic mantle; this hypothesis however requires high temperatures (more than 600 °C) and it thus cannot explain seismic events that occur at $T < 600$ °C^{1,3,24}. Stress amplification is instead proposed to occur in slab domains characterized by inner rheological contrasts²⁵. Local tectonics, bending stresses resulting from slab morphology, and the subduction rate may also control the pattern of intra-slab seismicity^{26,27}.

Outer-rise faults (or bending faults) form in a prominent bathymetric bulge seaward of the trench axis, after the flexure of the subducting lithosphere; the incoming plate records the strongest bending within 50 km of the trench axis^{28–30}. A direct correlation between outer-rise faults and intermediate earthquakes has been assumed by several authors^{31,32}, according to which seismic events are derived from the reactivation of shallow incoming plate faults.

Boneh et al.⁸ identified a statistically significant positive correlation between a data set of intermediate-depth global seismicity rates and the occurrence of shallow outer-rise normal faulting with large fault throw caused by plate bending. It has been therefore suggested that larger faults produce greater plate damage and a higher fluid circulation and hydration within the slab. As the result, the embrittlement of these intensely damaged and hydrated regions occurring at >70 km is in accordance with nucleation mechanisms for intermediate-depth earthquakes.

On the other hand, Warren et al.^{33,34} found that the rupture directivity of intermediate-depth earthquakes was inconsistent with the orientation of outer-rise normal faults.

Recently, Gerya et al.³⁵ demonstrated numerically that outer-rise normal faulting is a transient process, which leads to spontaneous segmentation of subducting slabs due to coupled brittle-ductile damage. Slab segmentation allowed to explain a number of subduction-related phenomena, including, in particular, the development of segmented seismic velocity anomalies in subducting slabs and the development of large offset normal faults at trenches³⁵. According to the newly proposed slab segmentation theory, the maximal normal faults throw grows with time (Gerya et al.³⁵, their Extended Data Fig. 6) and different subduction zones (or even different along-trench sections of the same subduction zone) can be characterized by different maturity of slab segmentation process and respectively by different magnitude of the maximal faults throw³⁵. This is in apparent contradiction with the proposal of Boneh et al.⁸ that the maximal faults throw magnitude observed at the surface is representative of the entire subducting slab and controls the intermediate depth seismicity rate of the slab. This contradiction is intriguing and calls for further analyses.

Here, we build on these findings in order to test whether or not the proposed transient slab segmentation process³⁵ can be reconciled with the observed positive correlation of the maximal outer rise faults throw and intermediate depth intra-slab seismicity rate⁸. Using our 2D numerical simulations of intraoceanic subduction, we demonstrate that many intraslab seismic events at intermediate depths (<200 km) could be correlated with transient episodes of stress increase within subducted intensely faulted and serpentinized slab segment boundaries. We moreover show that the stress increase occurs concurrently with either (i) transient outer-rise faults throw growth at the surface or (ii) transient episodes of interplate coupling.

Results

Outer-rise faults formation during subduction

The subduction process, which starts at the weak zone, evolves through time with the periodic formation of new faults in the slab, related to the flexure of the subducting oceanic lithosphere seaward of the trench axis.

Bending faults start to develop close to the trench: the main fault, with a dipping direction concordant to the subducting slab, generally develops taking advantage of pre-existing faults, even if it can also nucleate in the intact lithosphere. Secondary faults, concordant to the main fault, can form close to it. A set of antithetic faults later develops, finally forming a network of serpentinized faults in the subducting lithospheric mantle (Fig. 1).

Main and antithetic faults propagate deeply in the lithospheric mantle till about 25 km from the upper surface of the oceanic crust, dislocating the oceanic crust in a sort of graben-like structure, with fault throw growing with time (Supplementary Fig. 1). Large-offset normal faults localize spontaneously into narrow intensively deformed zones thereby producing the progressive segmentation of the slab as highlighted by Gerya et al.³⁵, with grain-size reduction being the key factor controlling this process³⁵. The subduction evolves in a slab rollover geometry when the lithosphere interacts with the lower-mantle boundary, defined by the perovskite phase transition.

Fluids-free episodic deviatoric stress increase among subducted bending faults

We observed that the deformation along these faults is always coupled with deviatoric stress increase in lithospheric domains among the newly formed brittle structures (Fig. 2). As soon as faults form at shallow depths, generally deviatoric stress is maximum at the bottom of faults networks, close to the junction point of main and antithetic faults (Supplementary Fig. 2). With subduction progress, the regions of lithosphere among deforming bending faults record a transient, local, stress increase, with the strain being localized along main and secondary faults. When deformation along these structures stops, inter faults undeformed rock sectors are no longer solicited, and stress decreases, suggesting that the local transient stress increase among faults is strictly correlated with deformation along faults.

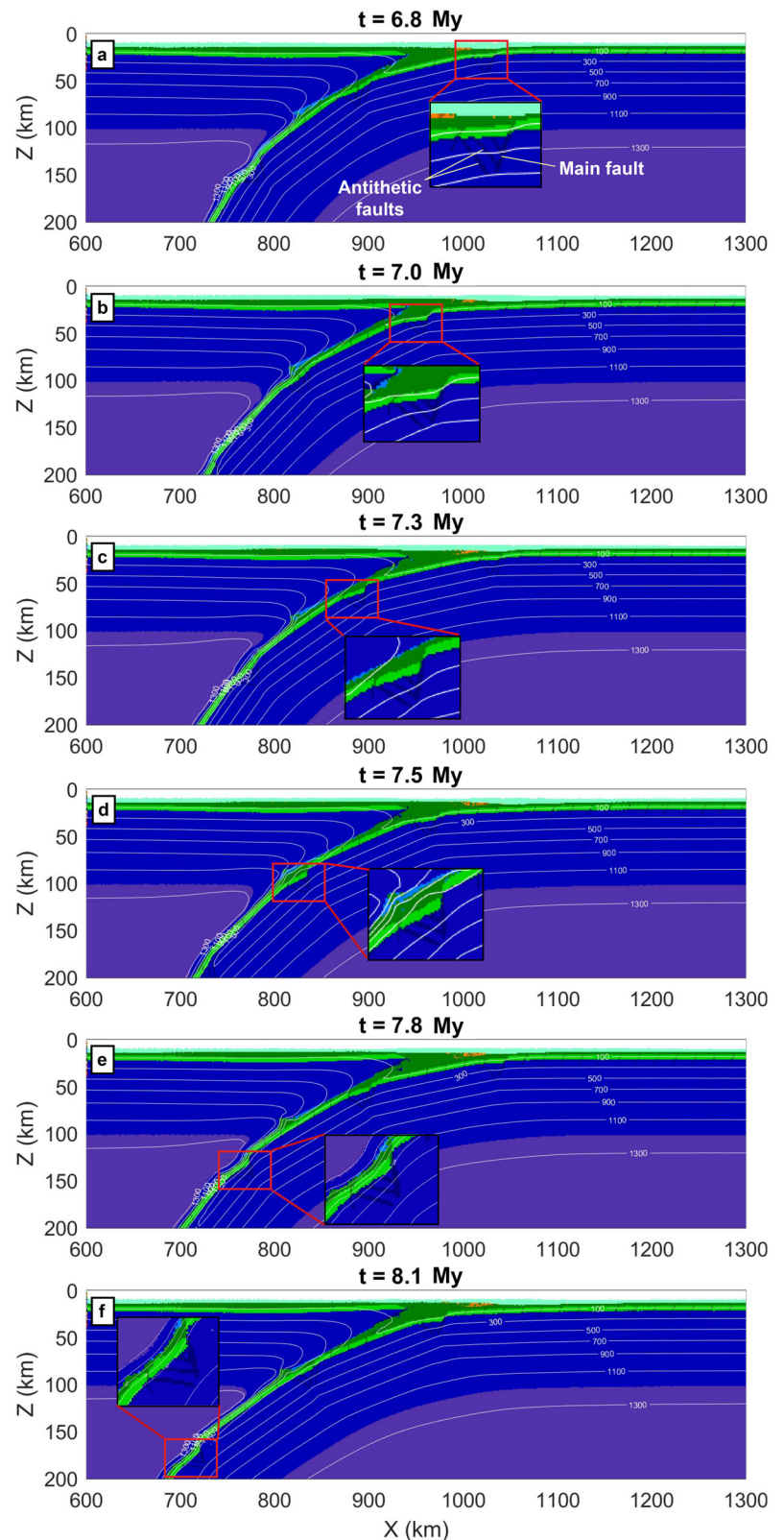
Episodes of transient stress increase in the slab are well visible following the fluctuation of deviatoric stress (S_{ii}) in rock volumes among outer-rise serpentinized faults (Fig. 2b–j). Average deviatoric stress evolution with time in these rock volumes is shown in Fig. 3. In order to minimize the effects of local spurious stress oscillations characteristic to particle in cell methods with strong local viscosity variations^{36,37}, we averaged deviatoric stress values over sufficiently large (50×50 km, i.e., 2500 grid cells, Fig. 2b–j) domains. We observed that several mechanisms can be responsible for spikes of average deviatoric stress in the slab during the subduction process:

(a) slab unbending (7.25 My from subduction initiation) or bending (7.81 My from subduction initiation), simultaneous to the formation of new faults networks at the outer rise; in our models unbending occurs before the complete interaction of the slab with the lower-mantle boundary; after this interaction, unbending regions are confined within about 100 km-depth; on the other side the deeper parts of the subducted crust undergo bending, following the evolving rollover geometry of the slab (Fig. 4).

(b) Episodic and local coupling between the shallow mantle wedge and the subducting plate (7.28, 7.32, and 7.54 My) (Figs. 3 and 5): interplate mechanical coupling occurs after the subduction of an oceanic plate with a rugged surface, that is a consequence of the formation of outer-rise faults with a large offset, producing “graben-like” structures in the downgoing lithosphere. The increase of interplate coupling causes a temporary slowdown of subduction velocity and a simultaneous, very localized, increase of deviatoric stress by up to >1 GPa level within the very narrow coupling region.

The above mechanisms trigger a variation in the distribution of tectonic stress in the subducting plate that causes the increase of stress at outer-rise fault networks, which are the place of greater weakness of the subducting lithosphere.

Fig. 1 | Some steps of the modeled intraoceanic subduction process, tracking the evolution of a new outer-rise faults network (reference model). **a** A main and antithetic serpentinized faults form in the oceanic lithosphere close to the trench. **b** The fault network enters the subduction zone and evolves in a graben-like structure. **c–f** Outer-rise faults are progressively buried at increasing depths while other faults develop at the surface. The lithologies are represented with different colors, as described in Supplementary Fig. 6. The red box highlights the evolution of the new fault network formed at the outer rise. White lines are isotherms ($^{\circ}\text{C}$); “ t ” is the time after subduction begins. Here the main fault develops along a pre-existing fault.



The age of the plates (30 or 80 My vs 40 My of the reference model—Supplementary Figs. 3 and 4) does not strongly influence the stress behavior, since its increase, either in younger or older slabs, follows the same trend as in the reference model. This parameter, however, controls the depths inside the slab at which stress can increase: in older slabs (80 My), a buildup of the stress can occur even at 35 km from the slab

surface, whereas in younger slabs (30 My) the stress can increase only till 25 km inside the slab. The age of the plates also affects the maximum temperature reached by serpentinized outer-rise faults: in older and colder slabs, in fact, faults reach a temperature slightly above 300 $^{\circ}\text{C}$, whereas in younger oceanic lithosphere faults are confined by the 500 $^{\circ}\text{C}$ isotherm.

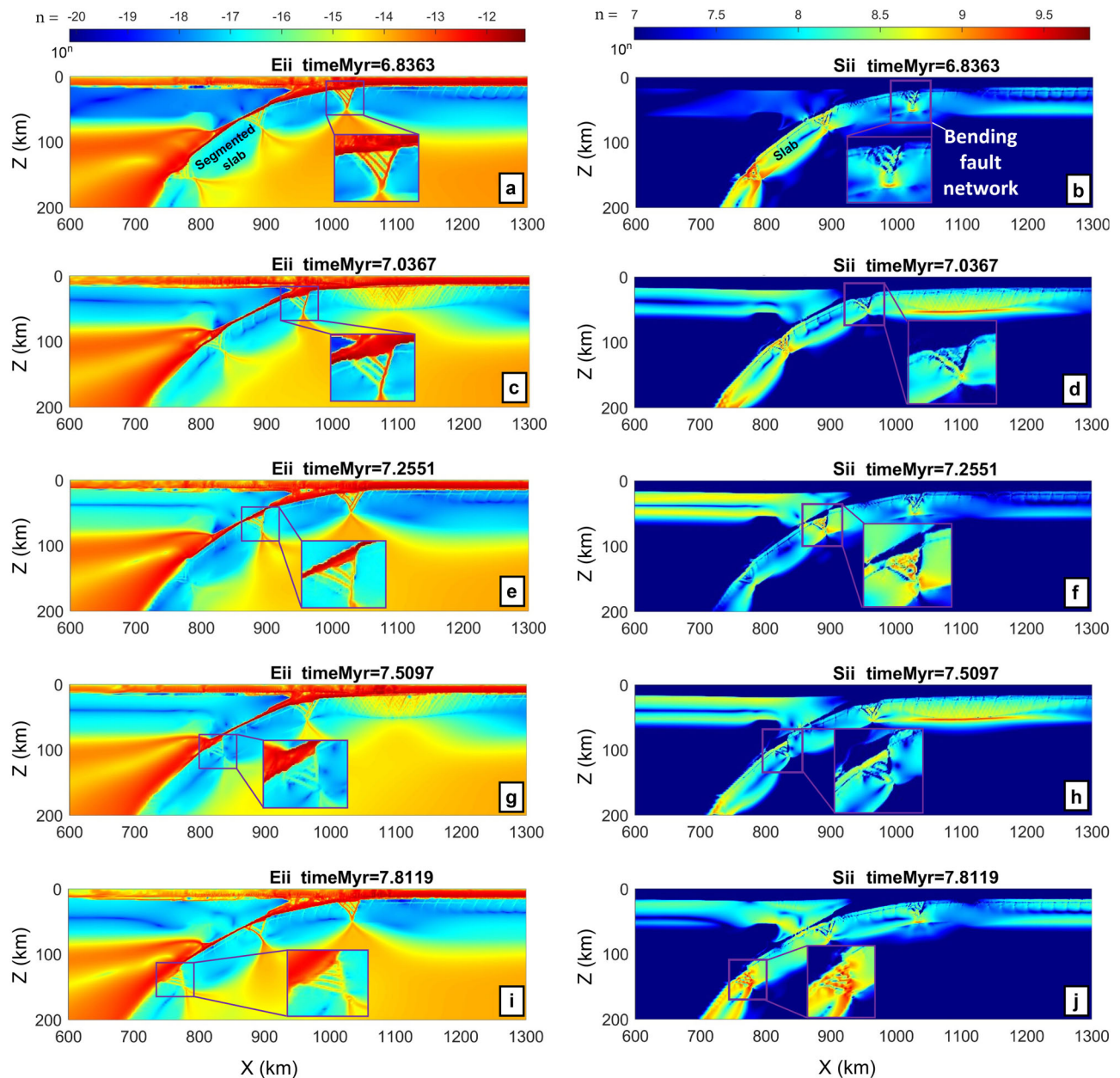


Fig. 2 | Strain rate vs deviatoric stress in the reference model. Strain rate ($\text{Log}(-\text{strain rate (s}^{-1}\text{)})$); left column) is compared with deviatoric stress ($\text{Log}(\text{stress (Pa)})$); right column). The evolution of a new outer-rise fault network is highlighted with the purple box. During the formation of main and antithetic faults close to the trench, the strain rate along the fault zones is maximum (a), and stress is focused at the bottom joint point of these structures (b). Approaching the subduction zone, strain predominantly affects the main fault (c), and stress increase progressively affects

wider volumes among faults (d). When a new fault network forms at the surface, strain affects both the subducted main and antithetic faults (e) and stress rises in inter-fault domains (f). With subduction progress, buried faults are only slightly deformed (g) and stress among them registers low values (h). The formation of new bending faults reactivates strain along the subducted faults (i) and inter-faults stress grows again (j).

Discussion

Bending faults in nature

The evolution of bending faults and their role in subduction have been already examined through numerical models in previous works^{22,35,38–40}. Moreover, the formation of bending faults and their role in arise alteration of the oceanic crust through the infiltration of water has been first postulated and then observed by several authors^{13,30,41–48}. The high degree of alteration and fracturation in outer rise regions has been evidenced by a notable reduction of compressional wave velocities in the mantle at several convergent margins, although an alternative hypothesis has also been proposed⁴⁹. For example, reduced velocities of the partially serpentinized mantle have been reported in subduction zones with little sediments such as

Northern Chile⁴⁶, Central Chile⁵⁰, and Central America^{30,51}, as well as in Southern Chile⁵². Local heat-flow anomalies also suggest that hydrothermal circulation is more vigorous where bend faults breach the seafloor and thus may govern fluid flow into the crust⁵³. Indeed, it is widely accepted the valuable role of outer rise faults in allowing the transportation of fluids in the lithosphere and in the deep mantle through the geochemical alteration of faults rocks^{30,38,41,48,54–58}.

It is well-known that the occurrence of fluids could support and enhance both fault reactivation, locally reducing their shear strength^{12,20}, and causing cracking of intact rocks: isolated pockets of fluids hosted in rock pores can nucleate microcracks; increasing strain would cause the interaction of the microcracks to produce crack arrays, that would extend and

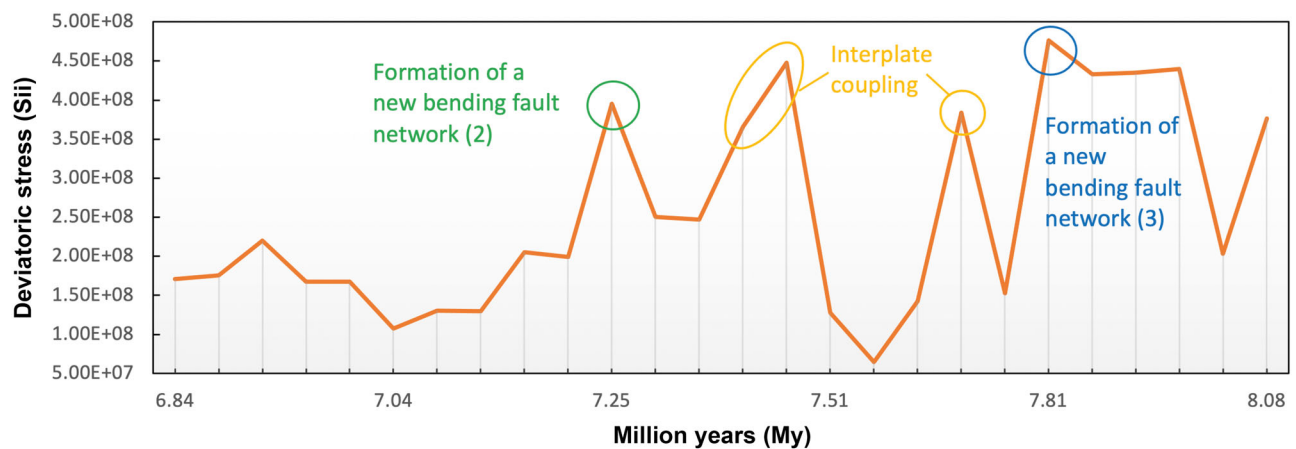


Fig. 3 | Plot of the mean value of the deviatoric stress. The mean value of deviatoric stress (S_{ii} —Log (deviatoric stress (Pa))) recorded in an area around a selected bending fault network (e.g., small purple box in Fig. 2b–j) is plotted. Colored ovals

depict stress spikes occurring concurrently either to the formation of new bending faults networks (2 and 3, green and blue ovals, respectively) or to episodes of interplate mechanical coupling (orange ovals).

coalesce²¹ and trigger rupture; the propagation of rupture through the water-filled microcracks would lead to substantial slip, stress drop and an earthquake¹².

In our reference model, brittle failure propagates down to about 25 km from the top of the slab and is confined within the 500 °C isotherm. In nature, embrittlement can, however, occur at higher temperatures⁵⁹, regardless of the presence of deep-water percolation⁴⁸; several authors suggest, in fact, that the brittle/ductile transition becomes deeper within the subducting plate with increasing depth in the mantle and can occur at temperature even around 600–800 °C^{16,48}. The temperature, at which brittle behavior can occur, seems controlled either by the age of the slab, in the presence of fluids (e.g., in a young slab brittle rheology could appear at a temperature greater than 500 ± 50 °C)²², or by the increase of the slab-pull forces (associated to the subduction of a relatively old, cold and heavy oceanic plate), even in a water-free environment⁴⁸.

Moreover, we observed that the depths reached by stress buildup depend on the plate age: older slabs are characterized by stress increase affecting deeper parts of the subducted oceanic lithosphere compared to younger slabs. This is in accordance with what observed in most subduction zone²³, where the distance between the upper and the lower planes of the DSZ increases with increasing slab age.

Dry outer-rise fault networks as sites for potential intermediate-depths earthquakes

In rock sectors undergoing a local stress increase, the occurrence of fluids released by dehydration reactions or preexisting fluids included in pores or microcracks could represent a contribution to reaching the brittle threshold of rocks, producing fracturing and possibly generating tremors or earthquakes.

The 2D simulations that we have run here show that the formation and the deformation of bending faults are accompanied by a local and transient increase of stress in lithosphere volumes surrounded by the newly formed fault network. In particular, we observed that this stress increase is strongly correlated with strain along serpentinized faults, i.e., stress increase occurs only when fault rocks are deformed and, therefore, re-activated by a perturbation given either by new bending faults formation or transient interplate coupling (Fig. 2).

Rock domains included in slab sectors among subducting bending faults, which are affected by transient stress increase, could represent volumes where potential rupture can occur, generating intraslab earthquakes, with/without the contribution of metamorphic reactions releasing fluids or mechanisms increasing fluid pressure. Indeed, the eventual occurrence of fluids in these domains could decrease the strength of already solicited rocks, promoting fracturing and eventual seismic events²².

We propose that fracturing, faulting and intraslab earthquakes can occur, other than along main and secondary serpentinized faults, also in volumes among them. The possible role of fluids in this process²², cannot be evaluated with our simplified numerical model. Intermediate-depths earthquakes occurring in dry rock volumes have also been proposed by field-based observations^{10,60,61}: as an example, Scambelluri et al.⁶¹ and Pennacchioni et al.⁶² found pseudotachylytes in dry lithospheric mantle domains banded by serpentinites, coherently exhumed from the eclogite facies conditions, testifying a seismic rupture occurring at intermediate depths.

We observed that stress build-up occurs during the formation of new bending fault networks at the outer rise or during episodic and local coupling between the shallow mantle wedge and the subducting plate; we, however, think that coupling, caused by structures on the subducting plate such as large-throw grabens, seamounts or oceanic plateau, could be only a secondary responsible for differential stress increase: it could be a very episodic mechanism, strongly related to the evolution of the morphology of the slab surface. Moreover, the volume of subducted sediments can play a major role in strongly influencing coupling: high sediment volumes at the subduction interface can, in fact, mask even a rugged morphology of the slab, inhibiting a possible interplate coupling and, thus, a build-up of the stress.

In general, earthquakes are expected to initiate in the cold core of the slab, where significant elastic stress can be maintained; rupture then propagates into a warmer, low-stress environment and this condition could be responsible for fault arrest^{63,64}: near the nucleation patch the stress drop might be locally large, but it could gradually decrease and become locally negative as rupture propagates, producing a small spatially averaged stress drop⁶⁵. Viscous weakening mechanisms, such as grain-size sensitive creep or flow of a melt layer, could possibly drive fault propagation in the slab^{64,66,67}. As underlined by Turner et al.⁶⁴, ruptures generating intermediate and deep earthquakes are mostly confined in regions where stress is potentially highest, with relatively low temperatures (lower than 1000 °C); this suggests that, regardless of their nucleation mechanisms, background stress exerts a first-order control on the propagation of intermediate and deep earthquakes, similar to what occurs for shallow earthquakes.

Moreover, it has been proven that, when across-strike fault interactions, other than, in example, regional tectonics, exert a stress-loading on faults, fault planes have more irregular stress patterns and interaction-influenced stress loading histories; the geometry of the fault/shear-zone system strongly controls stress-loading to failure in earthquakes⁶⁸.

We, therefore, suggest that dry rock volumes in serpentinized fault networks, where stress transiently increases, could represent sectors of potential rupture, where earthquakes can easily nucleate even without

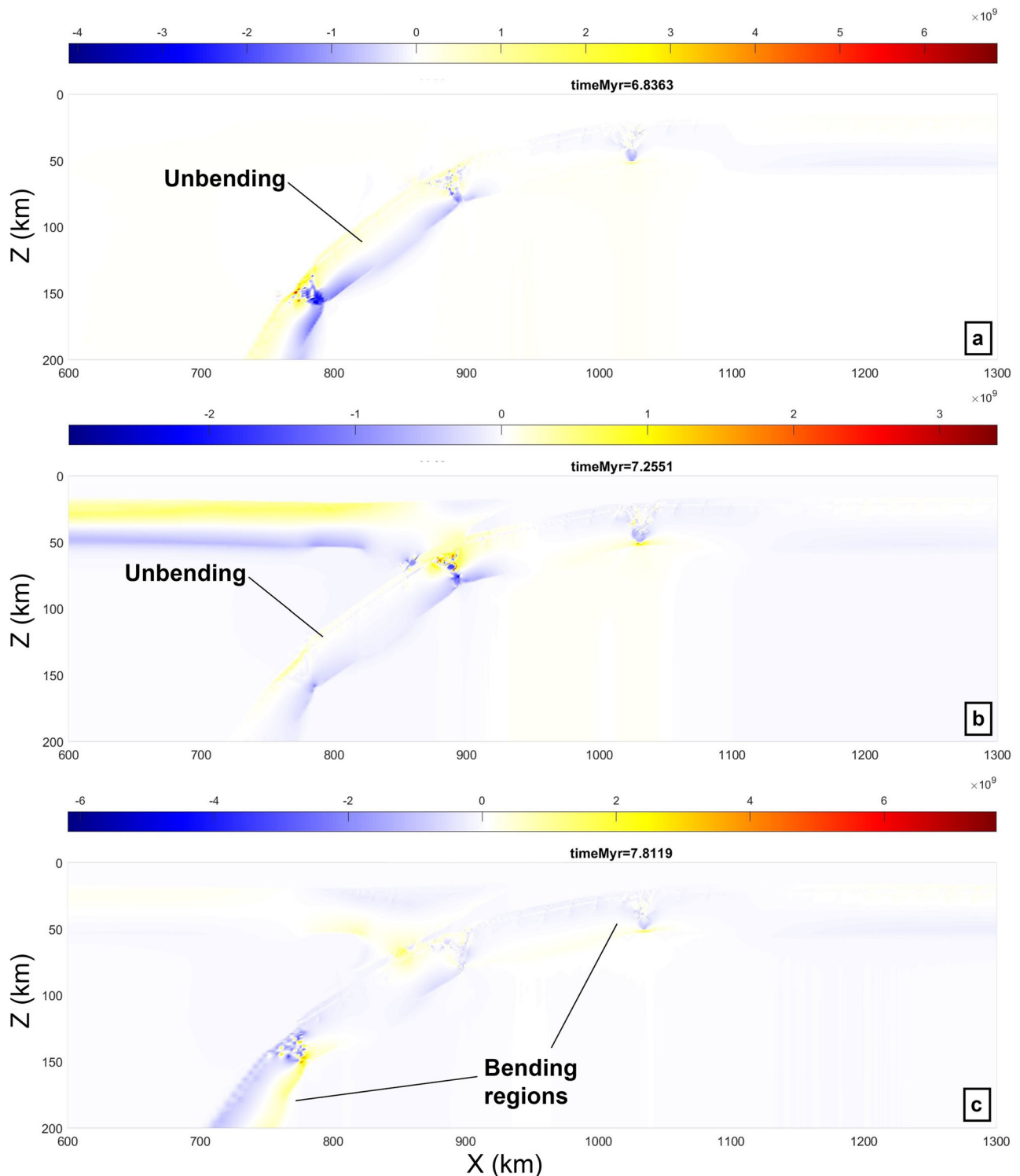


Fig. 4 | Areas of overpressure and underpressure (Pa) in the reference model. Unbending (a, b) and bending stages (c) of the slab are pointed out. Slab at depths greater than about 100 km starts to bend after its interaction with the lower-mantle boundary (c).

the possible contribution of dehydration reactions or fluids overpressure, underlining the major role of fault interaction in regulating the slab stress pattern and earthquakes triggering. Our findings are thus in accordance with the above-mentioned field-based evidence and with what proposed by Toffol et al.²⁵: using numerical modeling, they found that weak, circular-shaped flaws in the slab, which in nature could be represented by scattered serpentinized patches in meta-peridotite, behave as stress amplifiers in the strong dry slab. In these domains, high

deviatoric stresses, compatible with earthquake nucleation at intermediate depth, are reached in the region of slab unbending. Many authors observed that also the shape and the orientation of the heterogeneity, with respect to the far-field stresses, exert an important influence on the concentration of stress^{69–71}. In our simulations, outer-rise faults networks include serpentinized rocks (along the fault itself, with a general linear shape) that surround dry rock domains. The increase in deviatoric stress, that we observe in dry domains among serpentinized

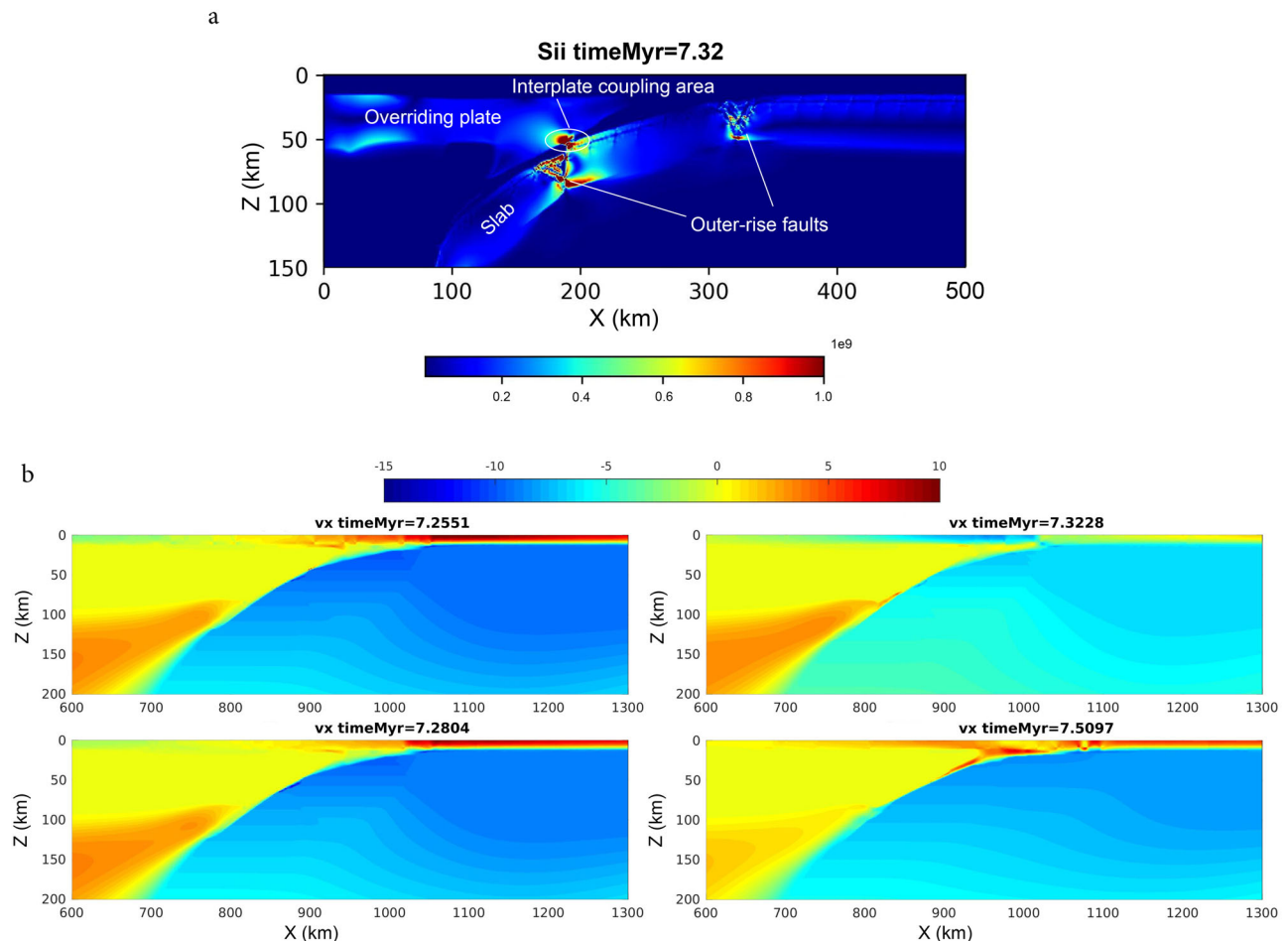


Fig. 5 | Coupling between the mantle wedge and the slab. a Deviatoric stress (Pa) showing mechanical coupling between the mantle wedge and the slab after the subduction of a large-throw graben, producing a stress build-up at the coupling region. Stress in slab region surrounding the subducted outer-rise faults is high compared to the other slab sectors. **b** Velocity along X direction ($\text{m s}^{-1} * 1\text{e}-9$), with

positive and negative values representing right-directed and left-directed movements, respectively. From 7.25 My till 7.32 My, the incoming plate records a velocity decrease related to the transient mechanical coupling between the upper mantle wedge and the downgoing slab.

faults, could thus be ascribed to a sort of stress amplification process related to the rheological contrast between weak serpentinized faults and the dry lithospheric mantle of the subducting plate. The stress build-up in mantle rocks and their possible rupture, concomitant with strain increase along outer-rise faults that we observed, could be the result of flow of a weaker material surrounding dry strong volumes causing strain incompatibility across the deforming system, as has been observed in lower crustal rocks^{72,73} and in numerical models of subduction zone mélanges⁷⁴.

The deep configuration of the slab in our simulations seems to partially influence the observed stress increase only in the mature stages of subduction (i.e., after the beginning of the interaction of the flattened leading edge of the slab with the underlying upper/lower mantle transition boundary) and only the deeper parts of the slab, since at least the shallower 100 km evolve independently and the fluctuation of stress values at outer-rise domains within this depth is independent of the evolution of the deep slab geometry.

The temporal coincidence of stress growth at intermediate depths and outer-rise faults throw growth at the trench, observed in our models, may also possibly explain the observed global positive correlation of intermediate-depth seismicity rate with maximal fault throw: what Boneh et al.⁸ observed in 17 subduction zones worldwide could represent the example in nature of our model steps in which we observe the gradual formation of outer-rise faults at the trench and the simultaneous intraslab

stress increase at subducted slab segment boundaries. The intermediated-depth seismic activity that Boneh et al.⁸ correlate with a massive fluid occurrence at highly-fractured bending regions could thus be related also to mechanisms observed in our models, such as slab unbending/bending and interplate mechanical coupling.

Our interpretations are supported by observations of intermediate depths seismic activity in the Pacific slab under Japan⁷⁵: it is found that intraslab earthquakes (magnitude 6.7–7.1) and their aftershock sequences generally occurred in lower seismic velocity zones within the subducting slab; these anomalies were attributed to heterogeneities in the slab and in particular to the occurrence of some pre-existing faults/fractures, where the dehydration of hydrous minerals, enhancing pore pressure increase, coupled with local tectonic and bending stresses, can cause intraslab events²⁶. The analogy between lower-velocity zones and pre-existing faults/fractures within the slab was highlighted also by Gerya et al.³⁵, which found that negative anomalies of velocity in the slab correspond to slab segment boundaries where outer-rise faults networks and grain-size reduction occur in some mature subduction zones.

The same behavior can be observed along some vertical cross-sections of P and S-wave tomography across northern Japan, where intraslab earthquakes focus preferably in slab portions affected by low-velocity anomalies (Supplementary Fig. 5): these regions could thus reflect the presence of serpentinized fractures and outer-rise faults, surrounding dry lithospheric mantle domains where stress build-up triggers seismic activity.

Methods

Numerical code specifications

The 2D numerical simulations shown here are based on the thermo-mechanical code I2VIS, which is built on the combination of a finite-difference method, applied on a staggered Eulerian grid, and a marker-in-cell technique^{76,77}. The momentum, mass, and energy conservation equations are solved on the Eulerian grid, and physical properties are transported by Lagrangian markers. Non-Newtonian, viscoplastic rheologies and variable thermal conductivity are used in the model^{78,79} (Supplementary Table 1), which includes major phase transitions in the oceanic crust and mantle, plus adiabatic, radiogenic, and frictional internal heating sources. The full details of this method can be found in Gerya & Yuen⁷⁶ and Gerya et al.³⁵

Initial model setup

The initial model setup replicates a segment of an oceanic basin, where spontaneous subduction initiation occurs at a weak zone in the mantle with a prescribed size^{80,81}. The simulated domain is 3000 × 3000 km along *x* and *y* directions (Supplementary Fig. 6), is resolved with an irregular rectangular grid of 1,261 × 511 nodes in the horizontal and vertical directions, respectively, and contains 19 million randomly distributed markers. The irregular grid resolution varies from 10 × 10 km at the model boundaries to 1 × 1 km in a 1000-km-wide and 200-km-deep subduction zone and outer-rise faulting area. Free-slip mechanical boundary conditions are applied to all sides of the model. A 12-km-thick ‘sticky’ air/water layer⁸² with low density (1 kg m⁻³ above 9 km, 1000 kg m⁻³ below 9 km) and viscosity (10¹⁷ Pa s) simulates the free-surface boundary condition atop the crust. Prescribing a laterally uniform cooling age and respective geotherm⁸³ with 273 K at the surface and a mantle potential temperature of 1523 K, it is possible to reproduce the initial thermal structure and thickness of the plate (Supplementary Fig. 6).

In the reference model (maaj), the oceanic plates have a uniform age of 40 My. Two supplementary models explore subduction dynamics considering a uniform age of either 30 (maat) or 80 My (maaq), respectively. In the asthenospheric mantle, an adiabatic gradient of 0.5 K km⁻¹ is initially prescribed (Supplementary Fig. 6).

In order to mimic the hot boundary layer at the core–mantle boundary, the temperature increases linearly by 744 K within 500 km at the lower boundary. For the mantle and the crust, a temperature-dependent thermal conductivity is used (Supplementary Table 1). The thermal boundary conditions at the top and at the bottom are 273 K and 3567–3717 K (depending on the mantle potential temperature), respectively, and zero heat flux on two other sides of the model.

The temperature of the ‘sticky’ air/water is kept constant at 273 K, in order to ensure efficient heat transfer from the surface of the crust. In the models, a gravitational acceleration of 9.81 m s⁻² has been used.

Horizontal plate motion is simulated by applying a prescribed constant velocity (i.e., about 5 cm/y) to a narrow high-viscosity area prescribed in the incoming subducting plate.

Erosion and sedimentation processes shape the top of the lithosphere, according to the following Eulerian transport equation⁷⁶:

$$\frac{\partial z_{es}}{\partial t} = v_z - v_x \frac{\partial z_{es}}{\partial x} - v_s + v_e, \quad (1)$$

where z_{es} is the vertical position of the erosion/sedimentation surface as a function of the horizontal distance x , x , and z are horizontal and vertical coordinates, respectively, v_s and v_e are the sedimentation and erosion rates, respectively, v_z and v_x are the vertical and horizontal components of the material velocity vector at the surface, respectively. The sedimentation and erosion rates are the following⁸⁴: $v_s = 0$ mm yr⁻¹ and $v_e = 0.3$ mm yr⁻¹ when $z < 9$ km (the sea level prescribed in the model), and $v_s = 0.03$ mm yr⁻¹ and $v_e = 0$ mm yr⁻¹, when $z > 9$ km. Considering the accumulated sedimentary prism, the maximal surface slope is limited by 17°.

Surface processes have however, in our numerical experiments, a relatively minor role in subduction dynamics and slab morphology.

These models consider two oceanic plates, separated by a weak zone in the mantle. The oceanic crust consists of a 3 km-thick layer of basalts overlying a 5 km-thick layer of gabbroic rocks. No initial sedimentary layer is prescribed in the reference model. In these experiments, inherited faults affect the oceanic crust and the shallow lithospheric mantle till 14 km from the oceanic crust surface. Faults are 1 km thick and are 20 km spaced; where they affect the basaltic and gabbroic layers, they have a weak (basaltic) rheology, whereas, in the mantle, they are represented by serpentinitic rocks and have an inclination of about 63° toward the trench. Serpentinization of outer-rise fault networks occurs when the mantle rocks reach the upper strain limit (γ_0). A serpentinite layer, 2 km thick, occurs at the base of the crust in the incoming plate, to simulate serpentinization of the mantle after the infiltration of fluids along inherited faults.

Density model

The extended Boussinesq approximation, with the incompressible continuity equation and variable density, has been implemented in the momentum and energy conservation equations. The following equation describes the variation of rock density with pressure (P) and temperature (T)

$$\rho_{P,T} = \rho_0 [1 - \alpha(T - T_0)][1 + \beta(P - P_0)], \quad (2)$$

where ρ_0 is the standard density at $P_0 = 1$ MPa and $T_0 = 298$ K, and $\alpha = 2 \times 10^{-5}$ K⁻¹ and $\beta = 4.5 \times 10^{-12}$ Pa⁻¹ are the coefficients of thermal expansion and compressibility, respectively (Supplementary Table 1).

We also considered the phase transformations of olivine into wadsleyite and ringwoodite⁸⁵ and into bridgmanite in the mantle⁸⁶. The linear increase of density in the crust with pressure, from 0% to 16%, in the P – T region between the experimentally determined garnet-in and plagioclase-out phase transitions in basalt⁸⁷ tries to reproduce the eclogitization of subducted basaltic and gabbroic crust. For density changes, stishovite and perovskite⁸⁶ transitions in the crust are also taken into account.

Viscoplastic rheological model

The evaluation of the effective viscosity of the material allowed the implementation of viscous and brittle (plastic) properties in the models (Supplementary Table 1). For the ductile rheology, the contributions from different flow laws such as dislocation and diffusion creep are taken into account by composite rheology for $\eta_{ductile}$:

$$\frac{1}{\eta_{ductile}} = \frac{1}{\eta_{diff}} + \frac{1}{\eta_{disl}} \quad (3)$$

where η_{diff} and η_{disl} are effective viscosities for diffusion and dislocation creep, respectively.

For the crust, constant grain size is assumed and η_{diff} and η_{disl} are computed as

$$\eta_{diff} = \frac{A}{2\sigma_{cr}^{n-1}} \exp\left(\frac{E + PV}{RT}\right) \quad (4)$$

$$\eta_{disl} = \frac{1}{2} A^{\frac{1}{n}} \exp\left(\frac{E + PV}{nRT}\right) \dot{\epsilon}_{II}^{\frac{1}{n}-1} \quad (5)$$

where T is the temperature (in K), P is pressure, R is the gas constant, $\dot{\epsilon}_{II} = \sqrt{1/2(\dot{\epsilon}_{ij})^2}$ is the square root of the second invariant of the strain rate tensor, σ_{cr} is the assumed diffusion–dislocation transition stress, and A , E , V , and n are the experimentally determined pre-exponential factor, activation energy, activation volume and stress exponent of the viscous creep, respectively (Supplementary Table 1).

Grain-size reduction and growth processes assisted by Zener pinning are also considered in the used ductile creep model for the mantle, and η_{diff} and η_{disl} are calculated according to references included in Gerya et al.³⁵ The rheology follows a composite law as in Eq.(1), wherein:

$$\eta_{diff} = \frac{1}{2} A_{diff} h^m \exp\left(\frac{E_{diff} + PV_{diff}}{RT}\right) \quad (6)$$

$$\eta_{disl} = \frac{1}{2} A_{disl}^{\frac{1}{n}} \exp\left(\frac{E_{disl} + PV_{disl}}{nRT}\right) \dot{\epsilon}_I^{\frac{1}{n}-1} \quad (7)$$

where h is the mean grain size and m is the grain-size exponent. The interplay between diffusion and dislocation creep is controlled by a grain-size-evolution equation dependent on the mechanical work and temperature. The grain-size evolution model is based on several assumptions. (1) Two well-mixed phases are present in the mantle peridotite: olivine and pyroxene, considered to have the same density and rheology, and have a fixed volume fraction of 60% and 40%, respectively. (2) In both phases, the relative motion is considered to be negligible, and therefore, their velocity is the same. (3) A self-similar log-normal distribution characterizes the grain-size distribution. Therefore, it always retains the same shape and its mean variance and amplitude are fully characterized by a unique grain size. (4) The system is in a state known as the pinned-state limit wherein the pinning of phases by each other controls the grain-size evolution (that is, Zener pinning is dominant)⁸⁸. The grain size is thus controlled by the roughness r of the interface between the two phases. A relation between the mean grain size h (sufficient to fully describe the system) and the roughness r is given by $h = \frac{r}{\sqrt{hg}}$, where $hg \approx \pi/2$ for the phase volume fraction in the models. The roughness evolution is described by the following equations⁸⁸⁻⁹¹:

$$\frac{dr}{dt} = \frac{\eta G_I}{qr^{(q-1)}} - \frac{f_I r^2}{\gamma_I \eta} \Psi \quad (8)$$

$$G_I = \frac{G_g}{G_{fac}} \frac{q}{p} r^{(q-p)} \quad (9)$$

$$G_g = A_g \exp\left(\frac{E_g + PV_g}{RT}\right) \quad (10)$$

$$f_I = f_0 \exp\left(-2\left(\frac{T}{1,000}\right)^{2.9}\right) \quad (11)$$

where G_I is the interface coarsening, G_g is the grain growth rate, $G_{fac} = 100$ is the grain growth rate factor, $p = 2$ is the grain-size coarsening exponent, $q = 4$ is the roughness coarsening exponent, $A_g = 2 \times 10^{(4-6p)}$ is the pre-exponential factor, γ_I is the surface tension, $E_g = 3 \times 10^5$ is the grain-growth activation energy, $V_g = V_{diff}$ is the grain-growth activation volume, f_I is the fraction of mechanical work Ψ converted to interface damage resulting in grain-size reduction; $f_0 = 0.001$ is the interface damage at 1000 K, and $\eta = 3\phi_{ol}\phi_{px}$ is interface area density depending on the volume fractions of olivine ($\phi_{ol} = 0.6$) and pyroxene ($\phi_{px} = 0.4$) in the mantle.

We implemented an effective viscous-plastic rheology combining ductile rheology with a brittle (plastic) rheology, where the following upper limit for the ductile viscosity is expressed as

$$\eta_{ductile} \leq \frac{C + \mu P}{2\dot{\epsilon}_{II}} \quad (12)$$

$$\mu = \mu_0 - \gamma\mu_y \text{ for } \gamma \leq \gamma_0 \text{ and } \mu = \mu_1 \text{ for } \gamma > \gamma_0,$$

$$\gamma = \int \sqrt{\frac{1}{2}(\dot{\epsilon}_{ij(plastic)})^2} dt \quad (13)$$

In the above equations, μ is the internal friction coefficient, μ_0 and μ_1 are the initial and final internal friction coefficient, respectively (Supplementary Table 1), $\mu_y = (\mu_0 - \mu_1)/\gamma_0$ is the rate of faults weakening with integrated plastic strain γ (γ_0 is the upper strain limit for the fracture-related weakening), t is time, $\dot{\epsilon}$ is the plastic strain rate tensor and C is the rock compressive strength at $P = 0$ (Supplementary Table 1). The mantle inside outer-rise normal faults that reached the upper strain limit (γ_0) is serpentinized and has the respective rheology (Supplementary Table 1).

Deriving fault throw from numerical simulations

Integrated plastic strain γ stored on markers has been considered the base of fault throw estimation in our numerical models: we first defined a reference surface located inside the rheologically strong gabbroic layer at a 3.5-km vertical distance above the oceanic Moho, in order to have a conservative estimate of the plastic strain related to normal faulting. We later averaged, at the nearest vertical grid lines intercepting this reference surface, strain on markers which were found within 250-m vertical distance around the reference surface. Faults are therefore defined by the local maxima of the plastic strain γ , for which an effective fault throw magnitude M was calculated as:

$$M = \gamma D \sin(\alpha) \quad (14)$$

where $D = 1$ km is a characteristic fault width in our models (as faults always localize within one grid cell) and α is the normal fault dip angle in the models. As the sensitivity threshold for this numerical approach, we have used a throw of 20 m.

Other specifics of model design and the numerical code are provided by Gerya et al.³⁵

Data availability

The authors declare that the data supporting the findings of this study are available at <https://doi.org/10.17605/OSF.IO/32H9A> and from the corresponding author on request.

Code availability

The authors declare that the C and Matlab codes used for numerical experiments and visualization are available at <https://doi.org/10.17605/OSF.IO/32H9A>.

Received: 4 October 2023; Accepted: 25 April 2024;

Published online: 13 May 2024

References

1. Kita, S. & Ferrand, T. P. Physical mechanisms of oceanic mantle earthquakes: comparison of natural and experimental events. *Sci. Rep. Nat.* **8**, 17049 (2018). 1-11.
2. Astiz, L., Lay, T. & Kanamori, H. Large intermediate-depth earthquakes and the subduction process. *Phys. Earth Planet. Inter.* **53**, 80-166 (1988).
3. Kelemen, P. B. & Hirth, G. A periodic shear-heating mechanism for intermediate-depth earthquakes in the mantle. *Nature* **446**, 787 (2007).
4. John, T. et al. Generation of intermediate-depth earthquakes by self-localizing thermal runaway. *Nat. Geosci.* **2**, 137-140 (2009).
5. Barcheck, C. G., Wiens, D. A., van Keken, P. E. & Hacker, B. R. The relationship of intermediate-and deep-focus seismicity to the hydration and dehydration of subducting slabs. *Earth Planet. Sci. Lett.* **349**, 153-160 (2012).
6. Prieto, G. A., Beroza, G. C., Barrett, S. A., López, G. A. & Florez, M. Earthquake nests as natural laboratories for the study of intermediate-depth earthquake mechanics. *Tectonophysics* **570-571**, 42-56 (2012).
7. Poli, P. & Prieto, G. A. Global rupture parameters for deep and intermediate-depth earthquakes. *J. Geophys. Res.* **121**, 8871-8887 (2016).

8. Boneh, Y. et al. Intermediate-depth earthquakes controlled by incoming plate hydration along bending-related faults. *Geophys. Res. Lett.* **46**, 3688–3697 (2019).
9. Zhan, Z. Mechanisms and implications of deep earthquakes. *Annu. Rev. Earth Planet. Sci.* **48**, 147–174 (2020).
10. Hosseinzadehsabeti, E., Ferré, E. C., Persaud, P., Fabbri, O. & Geissman, J. W. The rupture mechanisms of intraslab earthquakes: a multiscale review and re-evaluation. *Earth Sci. Rev.* **221**, 103782 (2021).
11. Kirby, S. H., Engdahl, E. R. & Denlinger R. in *Subduction: Top to Bottom, Geophysical Monograph Series*, Vol. 96 (eds Bebout G. E. et al.) 195–214 (AGU, 1996).
12. Davies, J. H. The role of hydraulic fractures and intermediate depth earthquakes in generating subduction zone magmatism. *Nature* **398**, 142 (1999).
13. Peacock, S. Are the lower planes of double seismic zones caused by serpentine dyhydration in subducting oceanic mantle?. *Geology* **29**, 299–302 (2001).
14. Ferrand, T. P. et al. Dehydration-driven stress transfer triggers intermediate-depth earthquakes. *Nat. Commun.* **8**, 15247 (2017).
15. Gasc, J. et al. Faulting of natural serpentinite: implications for intermediate depth seismicity. *Earth Planet. Sci. Lett.* **474**, 138–147 (2017).
16. Herrera, C. et al. Rupture properties of the 2020 M_w 6.8 Calama (northern Chile) intraslab earthquake. Comparison with similar intraslab events in the region. *Geophys. J. Int.* **232**, 2070–2079 (2023).
17. Poulet, T., Veveakis, E., Regenauer-Lieb, K. & Yuen, D. A. Thermo-poro-mechanics of chemically active creeping faults: 3. The role of serpentinite in episodic tremor and slip sequences, and transition to chaos. *J. Geophys. Res.* **119**, 4606–4625 (2014).
18. Malatesta, C., Federico, L., Crispini, L. & Capponi, G. Fluid-controlled deformation in blueschist-facies conditions: plastic vs brittle behaviour in a brecciated mylonite (Voltri Massif, Western Alps, Italy). *Geol. Mag.* **155**, 335–355 (2018).
19. Petrini, C. et al. Seismo-hydromechanical modelling of the seismic cycle: methodology and implications for subduction zone seismicity. *Tectonophysics* **791**, 228504 (2020).
20. Katayama, I., Terada, T., Okazaki, K. & Tanikawa, W. Episodic tremor and slow slip potentially linked to permeability contrasts at the Moho. *Nat. Geosci.* **5**, 731–734 (2012).
21. Du, Y. & Aydin, A. Interaction of multiple cracks and formation of echelon crack arrays. *Int. J. Numer. Anal. Methods Geomech.* **15**, 205–218 (1991).
22. Faccenda, M., Gerya, T. V., Mancktelow, N. S. & Moresi, L. Fluid flow during slab unbending and dehydration: implications for intermediate-depth seismicity, slab weakening and deep water recycling. *Geochem. Geophys. Geosyst.* **13**, Q01010 (2012).
23. Brudzinski, M. R., Thurber, C. H., Hacker, B. R. & Engdahl, E. R. Global prevalence of double Benioff zones. *Science* **316**, 1472–1474 (2007).
24. Ohuchi, T. et al. Intermediate-depth earthquakes linked to localized heating in dunite and harzburgite. *Nat. Geosci.* **10**, 771–776 (2017).
25. Toffol, G., Yang, J., Pennacchioni, G., Faccenda, M. & Scambelluri, M. How to quake a subducting dry slab at intermediate depths: inferences from numerical modelling. *Earth Planet. Sci. Lett.* **578**, 117289 (2022).
26. Mishra, O. P. & Zhao, D. Seismic evidence for dehydration embrittlement of the subducting Pacific slab. *Geophys. Res. Lett.* **31**, L09610 (2004).
27. Sandiford, D., Moresi, L., Sandiford, M. & Yang, T. Geometric controls on flat slab seismicity. *Earth Planet. Sci. Lett.* **527**, 115787 (2019).
28. Bondine, J. H. & Watts, A. B. On lithospheric flexure seaward of the Bonin and Mariana trenches. *Earth Planet. Sci. Lett.* **43**, 132–148 (1979).
29. Levitt, D. A. & Sandwell, D. T. Lithospheric bending at subduction zones based on depth soundings and satellite gravity. *J. Geophys. Res.* **100**, 379–400 (1995).
30. Grevemeyer, I., Ranero, C. R., Flueh, E. R., Kläschen, D. & Bialas, J. Passive and active seismological study of bending-related faulting and mantle serpentinization at the Middle America trench. *Earth Planet. Sci. Lett.* **258**, 528–542 (2007).
31. Ranero, C. R., Villaseñor, A., Phipps Morgan, J. & Weinrebe, W. Relationship between bend-faulting at trenches and intermediate-depth seismicity. *Geochem. Geophys. Geosyst.* **6**, Q12002 (2005).
32. Shillington, D. J. et al. Link between plate fabric, hydration and subduction zone seismicity in Alaska. *Nat. Geosci.* **8**, 961–964 (2015).
33. Warren, L. M., Hughes, A. N. & Silver, P. G. Earthquake mechanics and deformation in the Tonga-Kermadec subduction zone from fault plane orientations of intermediate- and deep-focus earthquakes. *J. Geophys. Res.* **112**, B05314 (2007).
34. Warren, L. M., Langstaff, M. A. & Silver, P. G. Fault plane orientations of intermediate-depth earthquakes in the Middle America Trench. *J. Geophys. Res.* **113**, B01304 (2008).
35. Gerya, T. V., Bercovici, D. & Becker, T. W. Dynamic slab segmentation due to brittle–ductile damage in the outer rise. *Nature* **246**, 245–250 (2021).
36. Duretz, T., May D. A., Gerya T. V., Tackley, P. J. Discretization errors and free surface stabilization in the finite difference and marker-in-cell method for applied geodynamics: a numerical study. *Geochem. Geophys. Geosyst.* **12**, Article Number: Q07004 (2011).
37. Yang, H., Moresi, L. N. & Mansour, J. Stress recovery for the particle-in-cell finite element method. *Phys. Earth Planet. Inter.* **311**, 106637 (2021).
38. Faccenda, M., Gerya, T. & Burlini, L. Deep slab hydration induced by bending-related variations in tectonic pressure. *Nat. Geosci.* **2**, 790–793 (2009).
39. Naliboff, J. B., Billen, M. I., Gerya, T. & Saunders, J. Dynamics of outer rise faulting in oceanic–continental subduction systems. *Geochem. Geophys. Geosyst.* **14**, 2310–2327 (2013).
40. Yang, J., Zhao, L. & Li, Y. Tectonic deformation at the outer rise of subduction zones. *Geophys. J. Int.* **232**, 1533–1544 (2023). March 2023.
41. Ranero, C. R., Morgan, J., Phipps, McIntosh, K. & Reichert, C. Bending, faulting, and mantle serpentinization at the Middle America trench. *Nature* **425**, 367–373 (2003).
42. Emry, E. L. & Wiens, D. A. Incoming plate faulting in the Northern and Western Pacific and implications for subduction zone water budgets. *Earth Planet. Sci. Lett.* **414**, 176–186 (2015).
43. Iyer, K., Rüpke, L. H., Phipps Morgan, J. & Grevemeyer, I. Controls of faulting and reaction kinetics on serpentinization and double Benioff zones. *Geochem. Geophys. Geosyst.* **13**, Q09010 (2012).
44. Key, K., Constable, S., Matsuno, T., Evans, R. L. & Myer, D. Electromagnetic detection of plate hydration due to bending faults at the Middle America Trench. *Earth Planet. Sci. Lett.* **351**, 45–53 (2012).
45. Nishikawa, T. & Ide, S. Background seismicity rate at subduction zones linked to slab-bending-related hydration. *Geophys. Res. Lett.* **42**, 7081–7089 (2015).
46. Ranero, C. R. & Sallares, V. Geophysical evidence for hydration of the crust and mantle of the Nazca plate during bending at the north Chile trench. *Geology* **32**, 549–552 (2004).
47. Tilmann, F. J., Grevemeyer, I., Flueh, E. R., Dahm, T. & Göbner, J. Seismicity in the outer rise offshore southern Chile: Indication of fluid effects in crust and mantle. *Earth Planet. Sci. Lett.* **269**, 41–55 (2008).
48. Cabrera, L. et al. Northern Chile intermediate-depth earthquakes controlled by plate hydration. *Geophys. J. Int.* **226**, 78–90 (2021).
49. Korenaga, J. On the extent of mantle hydration caused by plate bending. *Earth Planet. Sci. Lett.* **457**, 1–9 (2017).
50. Kopp, H., Flueh, E. R., Papenberg, C. & Klaeschen, D. Seismic investigations of the O’Higgins Seamount Group and Juan Fernández Ridge: aseismic ridge emplacement and lithosphere hydration. *Tectonics* **23**, TC2009 (2004).

51. Lefeldt, M., Grevemeyer, I., Göbner, J. & Bialas, J. Intraplate seismicity and related mantle hydration at the Nicaraguan trench outer rise. *Geophysical Journal International* **178**, 742–752 (2009).
52. Contreras-Reyes, E., Grevemeyer, I., Flueh, E. R., Scherwath, M. & Bialas, J. Effect of trench-outer rise bending-related faulting on seismic Poisson's ratio and mantle anisotropy: a case study offshore of Southern Central Chile. *Geophys. J. Int.* **173**, 142–156 (2008).
53. Naif, S., Key, K., Constable, S. & Evans, R. L. Water-rich bending faults at the Middle America Trench. *Geochem. Geophys. Geosyst.* **16**, 2582–2597 (2015).
54. Grevemeyer, I. et al. Heat flow and bending-related faulting at subduction trenches: case studies offshore Nicaragua and central Chile. *Earth Planet. Sci. Lett.* **236**, 238–248 (2005).
55. Grevemeyer, I., Ranero, C. R. & Ivandic, M. Structure of oceanic crust and serpentinization at subduction trenches. *Geosphere* **14**, 395–418 (2018).
56. Rüpke, L., Phipps Morgan, J., and Dixon, J. E. Implications of subduction rehydration for Earth's deep water cycle. in (eds Jacobsen, S. D., and Van Der Lee, S.) *Earth's Deep Water Cycle: American Geophysical Union Geophysical Monograph* 168, p. 263–276 (2009) <https://doi.org/10.1029/168GM20>.
57. van Keken, P. E., Hacker, B. R., Syracuse, E. M. & Abers, G. A. Subduction factory: 4. Depth- dependent flux of H₂O from subducting slabs worldwide. *J. Geophys. Res.* **116**, B01401 (2011).
58. Freundt, A. et al. Volatile (H₂O, CO₂, Cl, S) budget of the Central American subduction zone. *Int. J. Earth Sci.* **103**, 2101–2127 (2014).
59. Sippl, C., Schurr, B., Asch, G. & Kummerow, J. Seismicity structure of the northern Chile forearc from > 100,000 double-difference relocated hypocenters. *J. Geophys. Res.* **123**, 4063–4087 (2018).
60. Andersen, T. B. & Austrheim, H. Fossil earthquakes recorded by pseudotachylytes in mantle peridotite from the Alpine subduction complex of Corsica. *Earth Planet. Sci. Lett.* **242**, 58–72 (2006).
61. Scambelluri, M. et al. Fossil intermediate-depth earthquakes in subducting slabs linked to differential stress release. *Nat. Geosci.* **10**, 960–966 (2017).
62. Pennacchioni, G. et al. Record of intermediate-depth subduction seismicity in a dry slab from an exhumed ophiolite. *Earth Planet. Sci. Lett.* **548**, 116490 (2020).
63. Billen, M. I. Deep slab seismicity limited by rate of deformation in the transition zone. *Sci. Adv.* **6**, eaaz7692 (2020).
64. Turner, A. R. et al. Across-slab propagation and low stress drops of deep earthquakes in the Kuril subduction zone. *Geophys. Res. Lett.* **49**, e2022GL098402 (2022).
65. Noda, H., Lapusta, N. & Kanamori, H. Comparison of average stress drop measures for ruptures with heterogeneous stress change and implications for earthquake physics. *Geophys. J. Int.* **193**, 1691–1712 (2013).
66. Hirose, T. & Shimamoto, T. Growth of molten zone as a mechanism of slip weakening of simulated faults in gabbro during frictional melting. *J. Geophys. Res.* **110**, B05202 (2005).
67. Pozzi, G. et al. Coseismic fault lubrication by viscous deformation. *Nat. Geosci.* **14**, 437–442 (2021).
68. Sgambato, C., Phoebe, J., Walker, F., Mildon, Z. K. & Roberts, G. P. Stress loading history of earthquake faults influenced by fault/shear zone geometry and Coulomb pre-stress. *Nat. Sci. Rep.* **10**, 12724 (2020).
69. Eshelby, J. D. The elastic field outside an ellipsoidal inclusion. *Proc. R. Soc. Lond. Ser. A Math. Phys. Sci.* **252**, 561–569 (1959).
70. Moulas, E., Burg, J. P. & Podladchikov, Y. Stress field associated with elliptical inclusions in a deforming matrix: mathematical model and implications for tectonic overpressure in the lithosphere. *Tectonophysics* **631**, 37–49 (2014).
71. Schmid, D. W. & Podladchikov, Y. Y. Analytical solutions for deformable elliptical inclusions in general shear. *Geophys. J. Int.* **155**, 269–288 (2003).
72. Hawemann, F., Mancktelow, N. S., Pennacchioni, G., Wex, S. & Camacho, A. Weak and slow, strong and fast: How shear zones evolve in a dry continental crust (Musgrave Ranges, Central Australia). *J. Geophys. Res.* **124**, 219–240 (2019).
73. Campbell, L. R., Menegon, L., Fagereng, Å. & Pennacchioni, G. Earthquake nucleation in the lower crust by local stress amplification. *Nat. Commun.* **11**, 1322 (2020).
74. Beall, A., Fagereng, Å. & Ellis, S. Strength of strained two-phase mixtures: application to rapid creep and stress amplification in subduction zone mélange. *Geophys. Res. Lett.* **46**, 169–178 (2019).
75. Zhao, D. The 2011 Tohoku earthquake (Mw 9.0) sequence and subduction dynamics in Western Pacific and East Asia. *J. Asian Earth Sci.* **98**, 26–49 (2015).
76. Gerya, T. V. & Yuen, D. A. Characteristics-based marker-in-cell method with conservative finite-differences schemes for modeling geological flows with strongly variable transport properties. *Phys. Earth Planet. Inter.* **140**, 293–318 (2003).
77. Gerya, T. V. *Introduction to Numerical Geodynamic Modelling 2nd edn* (Cambridge Univ. Press) (2019).
78. Karato, S. & Wu, P. Rheology of the upper mantle: a synthesis. *Science* **260**, 771–778 (1993).
79. Hilairet, N. B. et al. High-pressure creep of serpentine, interseismic deformation, and initiation of subduction. *Science* **318**, 1910–1913 (2007).
80. Gerya, T. V., Connolly, J. A. D. & Yuen, D. A. Why is terrestrial subduction one-sided? *Geology* **36**, 43–46 (2008).
81. Malatesta, C. et al. Intraoceanic subduction of “heterogeneous” oceanic lithosphere in narrow basins: 2D numerical modeling. *Lithos* **140–141**, 234–251 (2012). May 2012.
82. Schmeling, H. et al. A benchmark comparison of spontaneous subduction models: towards a free surface. *Phys. Earth Planet. Inter.* **171**, 198–223 (2008).
83. Turcotte, D. L. & Schubert, G. *Geodynamics* (Cambridge Univ. Press, 2002).
84. Baitsch-Ghirardello, B., Gerya, T. V. & Burg, J.-P. Geodynamic regimes of intra-oceanic subduction: implications forearc extension vs. shortening processes. *Gondwana Res.* **25**, 546–560 (2014).
85. Katsura, T. & Ito, E. The system Mg₂SiO₄–Fe₂SiO₄ at high pressures and temperatures: precise determination of stabilities of olivine, modified spinel, and spinel. *J. Geophys. Res.* **94**, 663–670 (1989).
86. Ito, E. et al. Negative pressure–temperature slopes for reactions forming MgSiO₃ perovskite from calorimetry. *Science* **2J9** **1275**, 1278 (1990).
87. Ito, K. & Kennedy, G. C. *The Structure and Physical Properties of the Earth's Crust Geophysical Monograph Series* 14 (ed. Heacock, J. G.) 303–314 (American Geophysical Union, 1971).
88. Bercovici, D. & Ricard, Y. Mechanisms for the generation of plate tectonics by two- phase grain-damage and pinning. *Phys. Earth Planet. Inter.* **202–203**, 27–55 (2012).
89. Rozel, A., Ricard, Y. & Bercovici, D. A thermodynamically self-consistent damage equation for grain size evolution during dynamic recrystallization. *Geophys. J. Int.* **184**, 719–728 (2011).
90. Bercovici, D. & Ricard, Y. Generation of plate tectonics with two-phase grain-damage and pinning: source–sink model and toroidal flow. *Earth Planet. Sci. Lett.* **365**, 275–288 (2013).
91. Mulyukova, E. & Bercovici, D. Formation of lithospheric shear zones: effect of temperature on two-phase grain damage. *Phys. Earth Planet. Inter.* **270**, 195–212 (2017).

Acknowledgements

We are indebted with two anonymous reviewers and with a reviewer who signed as “Haibin @ ZJU”, that greatly improved the manuscript with important suggestions and comments. TG acknowledges support by SNF Research Grant 200021_192296 and by ILP Task Force “Bio-geodynamics of the Lithosphere”.

Author contributions

All authors contributed extensively to the work presented here. C.M. performed the numerical experiments and wrote the paper; T.G. elaborated the code of numerical models, provided computing resources, and acquired financial support for the project; S.P. analyzed the implications of model results; D.C. acquired financial support for the project. All authors discussed the results and reviewed and commented on the paper at all stages.

Competing interests

The authors declare no competing interests.

Additional information

Supplementary information The online version contains supplementary material available at <https://doi.org/10.1038/s43247-024-01420-9>.

Correspondence and requests for materials should be addressed to Cristina Malatesta.

Peer review information *Communications Earth & Environment* thanks Haibin Yang and the other, anonymous, reviewer(s) for their contribution to the peer review of this work. Primary Handling Editors: Carolina Ortiz Guerrero. A peer review file is available.

Reprints and permissions information is available at <http://www.nature.com/reprints>

Publisher's note Springer Nature remains neutral with regard to jurisdictional claims in published maps and institutional affiliations.

Open Access This article is licensed under a Creative Commons Attribution 4.0 International License, which permits use, sharing, adaptation, distribution and reproduction in any medium or format, as long as you give appropriate credit to the original author(s) and the source, provide a link to the Creative Commons licence, and indicate if changes were made. The images or other third party material in this article are included in the article's Creative Commons licence, unless indicated otherwise in a credit line to the material. If material is not included in the article's Creative Commons licence and your intended use is not permitted by statutory regulation or exceeds the permitted use, you will need to obtain permission directly from the copyright holder. To view a copy of this licence, visit <http://creativecommons.org/licenses/by/4.0/>.

© The Author(s) 2024